

# GAS DENSITY AND X-RAY SURFACE BRIGHTNESS PROFILES OF CLUSTERS OF GALAXIES FROM DARK MATTER HALO POTENTIALS: BEYOND THE ISOTHERMAL $\beta$ -MODEL

YASUSHI SUTO,<sup>1,2</sup> SHIN SASAKI,<sup>3</sup> AND NOBUYOSHI MAKINO<sup>4,5</sup>

Received 1998 March 9; accepted 1998 July 28

## ABSTRACT

We describe a theoretical framework to compute the cluster gas distribution in hydrostatic equilibrium embedded in a class of spherical dark matter halo potentials. Unlike the conventional isothermal  $\beta$ -model, the present method provides a physical basis to directly probe the shape of the dark matter halo from the observed X-ray surface brightness and temperature profiles of clusters of galaxies. Specifically, we examine the extent to which the resulting gas density and X-ray surface brightness profiles are sensitive to the inner slope of the dark matter halo density and other more realistic effects, including the self-gravity of the gas and the polytropic equation of state. We also discuss a practical strategy to apply the present methodology to the actual cluster profiles from future X-ray observations.

*Subject headings:* cosmology: theory — dark matter — galaxies: clusters: general — X-rays: galaxies

## 1. INTRODUCTION

The gas density profiles of X-ray clusters of galaxies are known to be approximated well by the empirical formula, the isothermal  $\beta$ -model:

$$n_g(r) = \frac{n_{g0}}{[1 + (r/r_c)^2]^{3\beta/2}}. \quad (1)$$

Theoretically, this is consistent with the observed indication that luminous member galaxies obey the King profile and the assumption of the hydrostatic equilibrium of cluster gas. The galaxies in clusters, however, constitute a very small fraction of the gravitational mass of the entire cluster because of the presence of dark matter. Recent high-resolution  $N$ -body/hydrodynamical simulations have strongly suggested that dark halos of cluster scales are described by a family of fairly universal density profiles. Navarro, Frenk, & White (1996, 1997, hereafter NFW) proposed a profile,

$$\rho_{DM}(r) = \frac{\delta_c \rho_{c0}}{(r/r_s)(1 + r/r_s)^2}, \quad (2)$$

where  $\rho_{c0}$  is the critical density of the universe at  $z = 0$ , and  $\delta_c$  and  $r_s$  are the concentration parameter and the scaled radius whose explicit fitting formulae as a function of the halo mass  $M$  and cosmological parameters are found in NFW.

This enables one to predict the profiles of the gas and the X-ray surface brightness. Our previous work (Makino, Sasaki, & Suto 1998, hereafter Paper I) examined the case of the NFW profile and found that the resulting gas density profile is very close to the empirical model in equation (1).

Higher resolution  $N$ -body simulations by Fukushima & Makino (1997), however, indicate that the inner density

profile of the halo is much steeper than the NFW profile above. This conclusion was confirmed later by a series of systematic  $N$ -body simulations by Moore et al. (1998). Evans & Collett (1997) show that under some constraints the density profile  $\propto r^{-4/3}$  becomes the stationary solution to the collisionless Boltzmann equation. Furthermore, in Paper I we assumed that the isothermality and the possible effect of the temperature profile were neglected. The present paper explores these effects in more details and provides several useful working formulae for the X-ray surface brightness profiles as well. In what follows we describe various theoretical formulations and do not attempt to compare with real observational data. The comparison with observations in this context has been performed by Makino & Asano (1999), Tamura (1998), Xu et al. (1998), and Markevitch et al. (1998). While all of their results indicate that the current observational data are consistent with the predictions in the universal density profile, the current data quality in the spatial resolution of X-ray surface brightness and temperature profiles is not sufficient in distinguishing from the empirical  $\beta$ -model in an unambiguous manner. In this respect, upcoming X-ray missions, including *AXAF* and *XMM*, should definitely provide us with the data suitable for that purpose. This is mainly why we do not attempt any tentative comparison with the currently available data, but rather present various theoretical predictions that will be useful for future data analysis.

The plan of the paper is as follows: in § 2 we describe a new series of analytical solutions for a family of density profiles of dark matter halos generalizing Paper I. Then we examine effects of self-gravity of the gas in § 3 and of nonisothermality by adopting polytropic equation of state in § 4. Finally, § 5 is devoted to discussion and conclusions.

## 2. ISOTHERMAL GAS AND X-RAY SURFACE BRIGHTNESS PROFILES FROM A FAMILY OF DARK MATTER HALO POTENTIALS

We generalize the NFW profile in equation (2) and consider a family of density profiles describing the dark matter halo:

$$\rho_{DM}(x) = \frac{\delta_c \rho_{c0}}{x^\mu(1 + x^\nu)^\lambda}, \quad (3)$$

<sup>1</sup> Department of Physics, University of Tokyo, Tokyo 113-0033, Japan; suto@phys.s.u-tokyo.ac.jp.

<sup>2</sup> Research Center for the Early Universe (RESCEU), School of Science University of Tokyo, Tokyo 113-0033, Japan.

<sup>3</sup> Department of Physics, Tokyo Metropolitan University, Hachioji, Tokyo 192-0397, Japan; sasaki@phys.metro-u.ac.jp.

<sup>4</sup> Department of Physics, Ritsumeikan University, Kusatsu, Shiga, 525-8577, Japan; makino@oita-ct.ac.jp.

<sup>5</sup> Present address: Department of Mechanical Engineering, Oita National College of Technology, 1666 Maki, Oita 870-0152, Japan.

where  $x \equiv r/r_s$  is the dimensionless radius in units of the characteristic scale  $r_s$ . Then the total mass of the dark matter halo within the radius  $r$  is given by

$$M(r) = 4\pi\delta_c \rho_{c0} r_s^3 m(r/r_s), \quad (4)$$

with

$$m(x) \equiv \int_0^x \frac{u^{2-\mu}}{(1+u^\nu)^\lambda} du. \quad (5)$$

If one neglects the gas and galaxy contributions to the gravitational mass, the gas density profile  $\rho_g(r)$  in hydrostatic equilibrium with the above dark matter potential satisfies

$$\frac{kT_g}{\mu_g m_p} \frac{d \ln \rho_g}{dr} = - \frac{GM(r)}{r^2}, \quad (6)$$

where  $\mu_g$  and  $m_p$  denote the mean molecular weight of the gas (we adopt 0.59 below) and the proton mass, and we assume that the gas temperature  $T_g$  is constant over the cluster (nonisothermal cases are considered in § 4). Equation (6) can be formally integrated to yield

$$\ln \frac{\rho_g(r)}{\rho_{g0}} = -B \int_0^{r/r_s} \frac{m(x)}{x^2} dx, \quad (7)$$

where

$$B \equiv \frac{4\pi G \mu_g m_p \delta_c \rho_{c0} r_s^2}{kT_g}. \quad (8)$$

Note that  $B$  is  $27b/2$  in terms of the parameter  $b$  defined in Paper I. Also,  $B$  is rewritten as

$$B = \frac{3}{\gamma m(1)} \frac{T_{\text{vir}}(r_s)}{T_g} \quad (9)$$

in terms of the virial temperature defined as

$$T_{\text{vir}}(r) \equiv \gamma \frac{G \mu_g m_p M(r)}{3kr}, \quad (10)$$

with  $\gamma (\approx 1-2)$  being a fudge factor (see Paper I).

With the density profile of the form in equation (3), equation (7) converges for  $\mu < 2$  and is rewritten as

$$\rho_g(r) = \rho_{g0} \exp [-Bf(r/r_s)], \quad (11)$$

where

$$f(x) \equiv \int_0^x \frac{m(u)}{u^2} du = \int_0^x \frac{u^{1-\mu}}{(1+u^\nu)^\lambda} du - \frac{1}{x} \int_0^x \frac{u^{2-\mu}}{(1+u^\nu)^\lambda} du. \quad (12)$$

In some specific cases, equations (5) and (12) are analytically integrated:

i)  $\mu = 1, \nu = 1, \lambda = 2$  (NFW):

$$m(x) = \ln(1+x) - \frac{x}{1+x}, \quad (13)$$

$$f(x) = 1 - \frac{1}{x} \ln(1+x). \quad (14)$$

ii)  $\mu = 3/2, \nu = 3/2, \lambda = 1$ :

$$m(x) = \frac{2}{3} \ln(1+x^{2/3}), \quad (15)$$

$$f(x) = \frac{x-2}{3x} \ln(1+\sqrt{x^3}) + \ln(1+\sqrt{x}) + \frac{2}{\sqrt{3}} \tan^{-1} \frac{2\sqrt{x}-1}{\sqrt{3}} + \frac{\sqrt{3}}{9} \pi. \quad (16)$$

iii)  $\mu = 3/2, \nu = 1, \lambda = 3/2$ :

$$m(x) = 2 \ln(\sqrt{x} + \sqrt{1+x}) - 2 \sqrt{\frac{x}{1+x}}, \quad (17)$$

$$f(x) = 2 \sqrt{\frac{1+x}{x}} - \frac{2}{x} \ln(\sqrt{x} + \sqrt{1+x}). \quad (18)$$

In what follows, we focus on the case with  $\mu = \alpha, \nu = 1, \lambda = 3 - \alpha$  ( $1 < \alpha < 2$ ). Then equation (12) reduces to

$$f(x) = \int_0^x \frac{u^{1-\alpha}}{(1+u)^{3-\alpha}} du - \frac{1}{x} \int_0^x \frac{u^{2-\alpha}}{(1+u)^{3-\alpha}} du. \quad (19)$$

If we set  $\alpha = 1$ , equation (19) reduces to case (i), which corresponds to the original proposal by Navarro et al. (1996, 1997) and is worked out in Paper I. Since the power-law slope of the inner region is very sensitive to the mass resolution limit of numerical simulations (Fukushige & Makino 1997; Moore et al. 1998; Melott et al. 1997; Splinter et al. 1998), we explore the similar profiles by changing  $\alpha$ . Since it is unlikely that the mass resolution limit affects the asymptotic outer halo profile  $\propto r^{-3}$ , we choose  $\lambda = 3 - \alpha$  to reproduce the asymptotic behavior.

### 2.1. Gas Density Profile

For  $1 \leq \alpha \leq 2$ , we numerically integrate equation (19) to compute the gas density profile, which is proportional to  $[F(x)]^B$ , where we define

$$F(x) \equiv \exp [-f(x)]. \quad (20)$$

Figure 1 plots the  $F(x)$  for  $\alpha = 1.0, 1.4$  and  $1.6$ , together with the empirical fit to the following function:

$$F_{\text{fit}}(x) = \left\{ 1 + \left[ \frac{x}{x_c(\alpha)} \right]^{q(\alpha)} \right\}^{p(\alpha)}. \quad (21)$$

For  $x \ll 1$ , equations (19)–(21) are consistent if

$$q(\alpha) = 2 - \alpha, \quad (22)$$

$$x_c^{2-\alpha} = (3 - \alpha)(2 - \alpha)p. \quad (23)$$

We adopt the relation (eq. [22]) but still keep  $p$  and  $x_c$  as two independent parameters to fit  $F(x)$  in the range of  $0.05 \leq x \leq 5$ . The results are plotted in solid lines in Figure 1. For  $1 < \alpha < 1.8$ , we find the following empirical fitting formulae:

$$x_c(\alpha) = 0.015(2 - \alpha)^{-2.5} + 0.47(2 - \alpha)^{0.5},$$

$$p(\alpha) = 0.33(2 - \alpha)^{-1.75}, \quad (24)$$

as plotted in Figure 2.

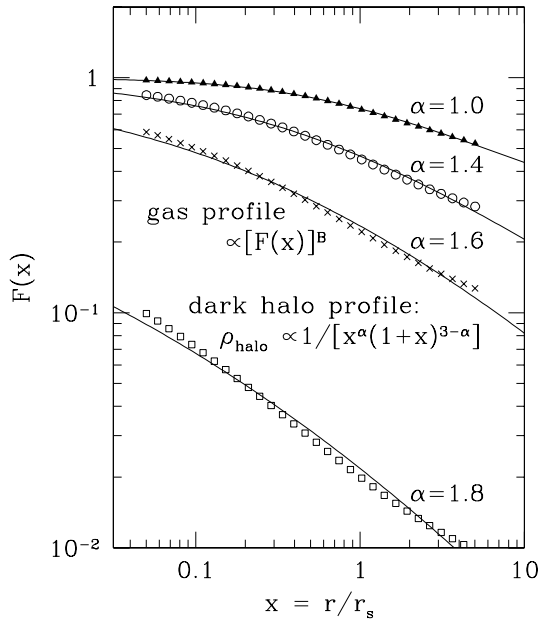


FIG. 1.—Gas density profiles predicted from a family of dark matter halo profiles. Solid triangles, open circles, crosses, and open squares indicate the results of numerical integrations for  $\alpha = 1.0, 1.4, 1.6$ , and  $1.8$ , respectively. Solid lines represent the best fits to eq. (21) with using eq. (24).

## 2.2. X-ray Surface Brightness Profile

From the observational point of view, it is more useful to compute the X-ray surface brightness profile on the sky:

$$\Sigma_x(\theta) \equiv \frac{1}{(1+z)^4} \int_{-\infty}^{\infty} \alpha_x(T_g) n_e^2(\sqrt{\theta^2 d_A^2(z) + l^2}) dl, \quad (25)$$

where  $z$  is the redshift of the cluster considered,  $\alpha_x$  is the X-ray (either bolometric or band-limited) emissivity,  $n_e(r)$  is the electron number density corresponding to the profile in

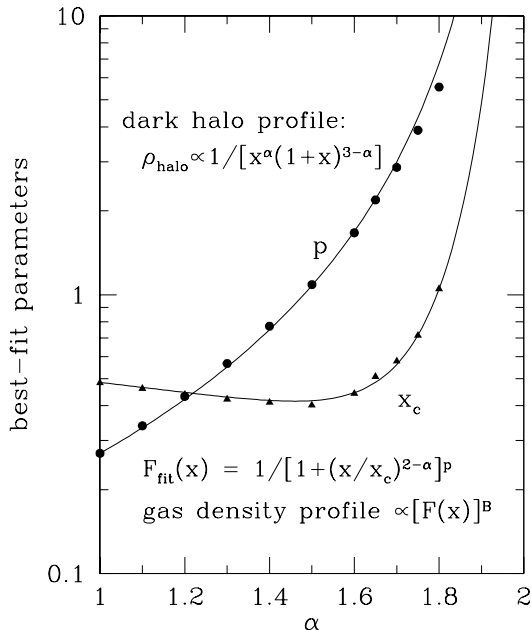


FIG. 2.—Best-fit parameters of  $x_c$  and  $p$  as a function of  $\alpha$ . Solid lines represent the fitting formula (eq. [24]), which is accurate for  $1.0 \leq \alpha \leq 1.6$ .

equation (11),  $d_A(z)$  is the angular diameter distance, and the integration is performed over the line of sight at an angular separation  $\theta$  from the center of the cluster.

Substituting the isothermal density profiles in equations (19) and (20), equation (25) reduces to

$$\Sigma_x(\theta) = \frac{2\alpha_x(T_g) n_{e0}^2 r_s}{(1+z)^4} S\left(\frac{\theta}{\theta_s}\right), \quad (26)$$

where  $\theta_s \equiv r_s/d_A(z)$ , and

$$S(\phi) \equiv \int_{\phi}^{\infty} \frac{x \exp[-2Bf(x)]}{\sqrt{x^2 - \phi^2}} dx. \quad (27)$$

Throughout the present paper we consider the X-ray bolometric emissivity and truncate the gas density at  $r = 20r_s$ , i.e.,  $n_g(r) = 0$  at  $r > 20r_s$ , in evaluating the surface brightness to avoid unphysical divergence. This is because  $20r_s$  is typically larger than the virial radius, and the gas profile should not be extended at the larger scale. We integrate equation (27) numerically for  $(\alpha, B) = (1.0, 10.0)$ ,  $(1.0, 20.0)$ ,  $(1.6, 5.0)$ , and  $(1.6, 10.0)$ , and the results are plotted in Figure 3. They cannot be reasonably fitted to the conventional  $\beta$ -model

$$S(\phi) = \frac{S(0)}{[1 + (\phi/\phi_{c,\beta})^2]^{3\beta-1/2}}, \quad (28)$$

where  $\beta$  is the slope parameter,  $\phi_{c,\beta}$  is the core radius, and  $S(0)$  is the central surface brightness. Because of the strong concentration of the dark matter halo in the present models, the resulting gas density profiles are also more concentrated than the conventional  $\beta$ -model. In fact, the deviation from the  $\beta$ -model becomes more appreciable for a larger  $\alpha$ . Rather, we find that the following generalized shape:

$$S(\phi) \propto \frac{1}{[1 + (\phi/\phi_c)^\xi]^\eta}, \quad (29)$$

with

$$\phi_c = 0.3 \left( \frac{2}{\alpha} - 1 \right), \quad (30)$$

$$\xi = 0.41 - 5.4(2 - \alpha)^6 + (0.585 + 6.47\alpha^{-5.18})B^{-\alpha/30}, \quad (31)$$

$$\eta = -0.68 - 5.09(\alpha - 1)^2 + (0.202 + 0.0206\alpha^8)B^{1.1}, \quad (32)$$

provides an excellent fit for  $5 \leq B \leq 20$  and  $1.0 \leq \alpha \leq 1.6$  in the range of  $10^{-4} \leq \phi \leq \phi_{\max}$ , where  $S(\phi_{\max}) = 10^{-4}S(0)$ .

Provided that the assumption of the isothermal gas is valid for actual clusters, our fitting formulae above can be used directly to probe the shape of the dark matter halo; fitting the observed X-ray surface brightness to equations (29)–(32) would result in the values of  $\alpha$ ,  $r_s$ , and  $B$  from the three fitted parameters  $\theta_s$ ,  $\phi_c$ ,  $\xi$ , and  $\eta$ . In addition, if the gas temperature  $T_g$  is measured from X-ray spectroscopic observations, the concentration parameter  $\delta_c$  is determined via equation (8).

Incidentally let us note that our fitting formulae (eq. [29]) are not unique in the sense that the three parameters  $\phi_c$ ,  $\xi$ , and  $\eta$  are correlated and written in terms of the two independent parameters  $\alpha$  and  $B$ . In particular,  $\phi_c$  and  $\xi$  are strongly correlated, and we would obtain an equally good fitting formula by changing these two appropriately. On the other hand,  $\eta$  is relatively insensitive to the choice of  $\phi_c$  or  $\xi$ .

Applying the procedure described above to three lensing clusters (A2163, A2218, and RX J1347.5–1145), Makino &

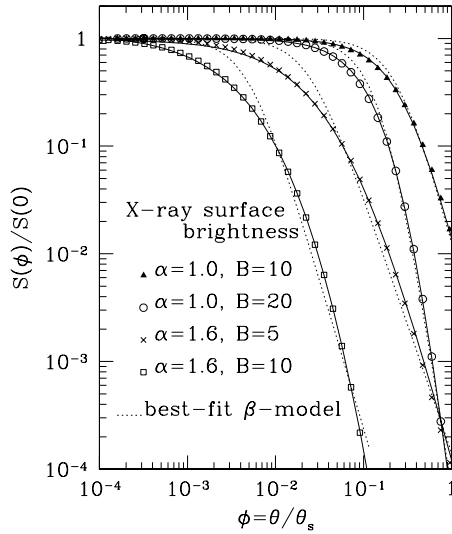


FIG. 3.—X-ray surface brightness profiles predicted from a family of dark matter halo profiles. Filled triangles, open circles, crosses, and open squares indicate the results of numerical integrations for  $(\alpha, B) = (1.0, 10.0)$ ,  $(1.0, 20.0)$ ,  $(1.6, 5.0)$ , and  $(1.6, 10.0)$ . Solid lines represent the best fits to eq. (29) with eqs. (30)–(32), while dotted lines indicate the best fits to the conventional  $\beta$ -model (eq. [28]).

Asano (1999) showed that the dark matter profile with  $\alpha \leq 1.4$  is consistent with the *ROSAT* HRI X-ray surface brightness profiles and that  $\alpha \sim 1.4$  is preferred in order for the X-ray mass estimate to be consistent with their giant arcs. Tamura (1998) also reached the similar conclusion on the basis of *ASCA/ROSAT* observation of A1060.

### 3. EFFECT OF SELF-GRAVITY OF THE GAS DENSITY DISTRIBUTION

When one properly includes the self-gravity of the gas distribution, equation (6) reads as

$$\frac{kT_g}{\mu_g m_p} \frac{d \ln \rho_g}{dr} = - \frac{GM_{\text{tot}}(r)}{r^2} = - \frac{4\pi G}{r^2} \int_0^r u^2 [\rho_{\text{DM}}(u) + \rho_g(u)] du. \quad (33)$$

With the profile of equation (3) for the dark matter halo, the above equation is rewritten in a nondimensional form as

$$\frac{dg(x)}{dx} = - \frac{B}{x^2} \int_0^x \left[ \frac{1}{u^\mu (1+u^\nu)^\lambda} + R e^{g(u)} \right] u^2 du, \quad (34)$$

where we introduce

$$g(x) \equiv \ln [\rho_g(x)/\rho_{g0}], \quad R \equiv \rho_{g0}/(\delta_c \rho_{c0}). \quad (35)$$

For  $\mu = \alpha$ ,  $\nu = 1$ , and  $\lambda = 3 - \alpha$ , the lowest order perturbation solution for equation (34) at  $x \ll 1$  is

$$g(x) \approx - \frac{B}{(3-\alpha)(2-\alpha)} x^{2-\alpha}. \quad (36)$$

In Figure 4 we consider the effect for the NFW profile ( $\alpha = 1$ ) only and numerically integrate the second-order differential equation

$$\frac{d^2 g(x)}{dx^2} + \frac{2}{x} \frac{dg(x)}{dx} + B \left[ \frac{1}{x(1+x)^2} + R e^{g(x)} \right] = 0, \quad (37)$$

where we rewrite equation (34) with the boundary condition specified from equation (36). The range of  $R$  is chosen so

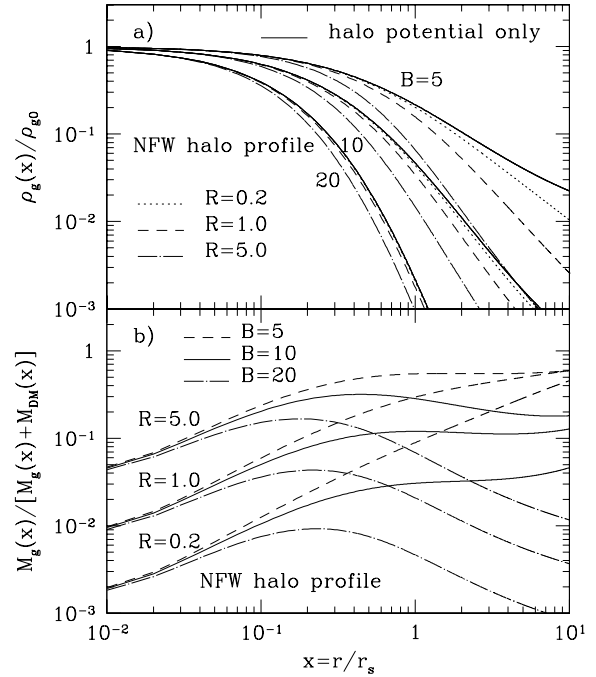


FIG. 4.—Effect of self-gravity of gas density distribution. (a) Gas density profile normalized in units of the central value. (b) Gas mass fraction. All models assume  $\alpha = 1$  (NFW profile).

that the resulting gas-to-dark halo ratio,

$$f_g(x) \equiv \frac{M_g(x)}{M_{\text{DM}}(x)} = \frac{R}{\ln(1+x) - x/(1+x)} \int_0^x e^{g(u)} u^2 du, \quad (38)$$

approximately ranges  $10^{-3}$ – $10^{-1}$  at  $x = 10$ .

We plot the gas density profiles, including the effect of self-gravity, in Figure 4a. With the increase of the gas fraction,  $R$ , the gas density profile becomes steeper at large radii, where the self-gravity of gas becomes significant compared with that of dark matter and confines the gas itself more strongly. Also, as  $B$  increases the gas distribution becomes more centrally concentrated, since the gas temperature  $T_g$ , and therefore the pressure gradient against the gravity, becomes smaller for larger  $B$ .

In Figure 4b we present the gas mass fraction ( $= M_g/[M_g + M_{\text{DM}}]$ ) for various values of  $B$  and  $R$ . At  $x \lesssim 1$ ,  $\rho_{\text{DM}}$  is proportional to  $r^{-1}$ , while  $\rho_{\text{gas}}$  is approximately constant. So the gas fractions of clusters in the present models increase roughly in proportion to  $x$  in the inner region. For larger  $x$ , on the other hand, the behavior is sensitive to the values of  $B$  and  $R$ . The observed baryon fraction of 0.1–0.2 of clusters indicates that  $(B, R) = (10, 5)$  and  $(5, 1)$  fall in an observationally relevant range. In this case, the effect of gas self-gravity is not significant but cannot be fully neglected, either. Also note that the gas mass fraction does not level off anywhere. Since the gas mass fraction provides an important constraint on the density parameter  $\Omega_0$  (e.g., White et al. 1993), this indicates the need for the quantitative comparison on the basis of the numerical integration of the above equation. As is discussed in § 5, this methodology is feasible under the generalized halo potential model.

### 4. EXAMPLE OF NONISOTHERMAL DISTRIBUTION: POLYTROPIC EQUATION OF STATE

In the discussion above, we have assumed the isothermal gas distribution. Although this is regarded as a reasonable

approximation to the actual clusters, it is true that some clusters do show nonisothermal features. In particular, Markevitch et al. (1998) reported that the temperature profiles of clusters appear remarkably similar and are approximately described by a polytrope with the polytropic index  $\Gamma = 1.2\text{--}1.3$  assuming that the gas density profile is given by the  $\beta$ -model. In this section we consider the effect of nonisothermal gas distribution on the basis of the polytropic equation of state for definiteness. More specifically, we adopt the following form for the gas pressure  $P$ :

$$P = P_0(\rho_g/\rho_{g0})^{1+1/n}, \quad (39)$$

or, equivalently, for the gas temperature:

$$T_g = T_{g0}(\rho_g/\rho_{g0})^{1/n}, \quad (40)$$

where the subscript 0 denotes the value at the center ( $x = 0$ ), and the polytropic index  $\Gamma$  is equal to  $1 + 1/n$ .

As before, we assume that the gas is in hydrostatic equilibrium,

$$\frac{1}{\rho_g} \frac{dP}{dr} = - \frac{GM(r)}{r^2}, \quad (41)$$

and neglect the self-gravity of the gas density. Define the function  $\epsilon(x)$ ,

$$\epsilon(x) \equiv [\rho_g(x)/\rho_{g0}]^{1/n} = T_g(x)/T_{g0}, \quad (42)$$

then equation (41) is written in a dimensionless form as

$$\frac{d\epsilon}{dx} = -B_p \frac{m(x)}{x^2}, \quad (43)$$

where the constant  $B_p$  is defined as

$$B_p \equiv \frac{4\pi G}{n+1} \frac{\mu_g m_p \rho_{c0} \delta_c r_s^2}{k T_{g0}} = \frac{B}{n+1}. \quad (44)$$

Note that as in equation (9)  $B_p$  is related to  $T_{\text{vir}}(r_s)$  as

$$B_p = \frac{3}{(n+1)\gamma m(1)} \frac{T_{\text{vir}}(r_s)}{T_{g0}}. \quad (45)$$

Equation (43) is integrated using the function  $f(x)$  (eq. [12]) to yield

$$\epsilon(x) = 1 - B_p f(x). \quad (46)$$

Throughout the rest of this section we consider the NFW profile only for illustration, but the discussion below can be easily generalized to other profiles.

The temperature and gas profiles in the present polytropic model are determined by specifying the two parameters,  $B_p$  and  $n$ . It should be noted that the upper limit on  $B_p$  is set by the maximal extension of the cluster gas; if the gas extends up to  $x = x_{\text{max}}$ , then

$$B_p < B_{p,\text{max}} \equiv 1/f(x_{\text{max}}). \quad (47)$$

In the case of the NFW profile,  $B_{p,\text{max}}$  are 1.32, 1.18, and 1 for  $x_{\text{max}} = 10, 20$ , and  $\infty$ , respectively. With equation (45), the above condition (eq. [47]) can be translated to the lower limit on the central gas temperature as

$$T_{g0} > \frac{3T_{\text{vir}}(r_s)}{(n+1)\gamma B_{p,\text{max}} m(1)} \sim \frac{15T_{\text{vir}}(r_s)}{(n+1)\gamma}. \quad (48)$$

The resulting temperature and gas profiles are plotted in Figure 5. Note that  $T_g(x)/T_{g0}$  is determined by  $B_p$  and the

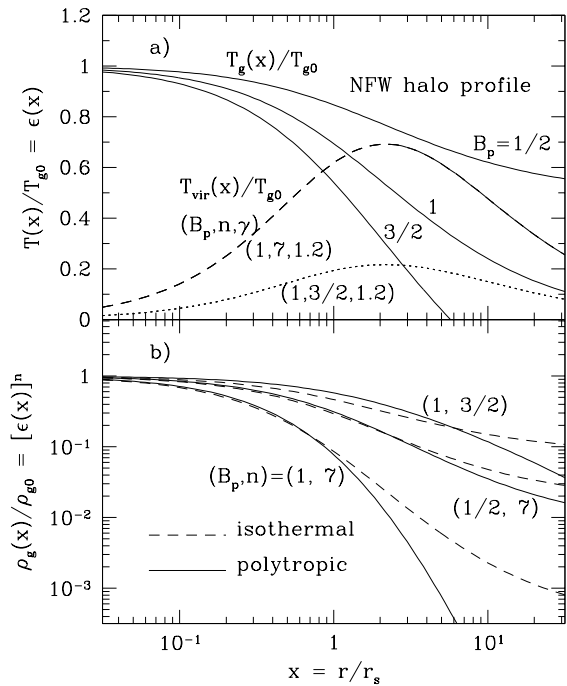


FIG. 5.—Profiles of temperatures and densities for polytropic models embedded in the NFW dark matter halo potential ( $\alpha = 1$ ). (a) Gas temperatures  $T_g$  are plotted in solid lines for  $B_p = 0.5, 1.0$ , and  $1.5$ . For reference, the virial temperature  $T_{\text{vir}}$  is plotted in dashed and dotted lines for  $(B_p, n, \gamma) = (1.0, 7, 1.2)$  and  $(1.0, 3/2, 1.2)$ , respectively. All values are in units of the central gas temperature  $T_{g0}$ . (b) Gas densities  $\rho_g$  for polytropic models (solid lines) and for the corresponding isothermal models (dashed lines) with  $B = (n+1)B_p$  in units of the central value  $\rho_{g0}$ .

halo shape parameters only and is independent of the value of  $n$ , while the resulting gas density profile is sensitive to  $n$ . The gas temperature in the present models starts to decrease appreciably around at  $x \gtrsim 1$  (Fig. 5a, solid lines), where the density profile departs significantly from that in the corresponding isothermal model (Fig. 5b, dashed lines). The virial temperature of the halo  $T_{\text{vir}}(x)$  is significantly different from the gas temperature  $T_g(x)$  in the present models (also in the isothermal model), indicating the importance of the detailed numerical simulations (e.g., Eke, Navarro, & Frenk 1998; Bryan & Norman 1998; Yoshikawa, Itoh, & Suto 1998) in predicting the temperature profile of clusters even in the present context.

Figure 6 shows the mass profile and gas mass fraction for polytropic models in comparison with those for isothermal cases. The gravity of gas mass is neglected, and for definiteness we choose the gas mass to be 10% of that of the dark halo at  $x = 10$ , which roughly corresponds to the virial radius in the NFW model.

The X-ray surface brightness and the emission-weighted temperature profiles on the sky,  $\Sigma_X(\theta)$  and  $T_X(\theta)$ , are defined by equation (25) and

$$T_X(\theta) \equiv \frac{\int_{-\infty}^{\infty} T_g \alpha_X(T_g) n_e^2 [\sqrt{\theta^2 d_A^2(z) + l^2}] dl}{\int_{-\infty}^{\infty} \alpha_X(T_g) n_e^2 [\sqrt{\theta^2 d_A^2(z) + l^2}] dl}, \quad (49)$$

respectively. If we consider the bolometric thermal bremsstrahlung emissivity only, the polytropic models we described above yield

$$\frac{\Sigma_X(\phi)}{\Sigma_X(0)} = \frac{\int_{\phi}^{\infty} x [\epsilon(x)]^{2n+1/2} \sqrt{x^2 - \phi^2} dx}{\int_0^{\infty} [\epsilon(x)]^{2n+1/2} dx}, \quad (50)$$

$$\frac{T_X(\phi)}{T_X(0)} = \frac{\int_{\phi}^{\infty} x [\epsilon(x)]^{2n+3/2} / \sqrt{x^2 - \phi^2} dx}{\int_{\phi}^{\infty} x [\epsilon(x)]^{2n+1/2} / \sqrt{x^2 - \phi^2} dx} \times \frac{\int_0^{\infty} [\epsilon(x)]^{2n+1/2} dx}{\int_0^{\infty} [\epsilon(x)]^{2n+3/2} dx}, \quad (51)$$

where  $\phi = \theta/\theta_s$  (§ 2.2). These profiles are plotted in Figure 7. The dotted curves in the upper panel indicate the best-fit  $\beta$ -model to the surface brightness. It is somewhat surprising that the X-ray surface brightness profiles for some models, e.g., with  $(B_p, n) = (1.0, 7.0)$ , are well approximated by the  $\beta$ -model despite the fact that the cluster is far from isothermal. It should also be noted here that the projected emission-weighted temperature  $T_X(\theta)$  systematically differs from the gas temperature  $T_g(r)$  evaluated at  $\theta = r/d_A$  (e.g., Figs. 5a and 7b).

### 5. DISCUSSION AND CONCLUSIONS

In this paper, we have presented a physical methodology to confront the dark matter halo mass distribution with the observed X-ray surface brightness profiles of the galaxy cluster. Unlike the previous phenomenological prescriptions including the isothermal  $\beta$ -model, this approach enables one to determine the dark matter halo profile directly from the observational data. This works in an especially straightforward manner when the cluster is well approximated as isothermal; then our fitting formulae (eqs. [24], [31], [32]) explicitly link the gas density and X-ray surface brightness profiles to the underlying dark matter halo potential as long as the halo is described by a family of profiles (eq. [3]). In § 4 we have described a prescription of computing the gas, temperature, and X-ray surface brightness profiles for clusters with polytropic equation of state. We confirm that the self-gravity of the gas does not affect the density profile significantly (§ 3) in the halo profiles considered throughout the paper. Incidentally, Bardelli et al. (1996) claimed that the gas mass fraction in A3558 (Shapley 8) is  $\sim 0.7$  at the Abell radius (assuming  $H_0 = 50 \text{ km s}^{-1} \text{ Mpc}^{-1}$ ). If confirmed, the X-ray surface brightness profile for such clusters should be computed while properly taking account of the self-gravity of gas, which is in fact feasible, as is shown below.

When both the self-gravity of gas density and the polytropic equation of state are taken into account, our procedure described in the present paper is generalized as follows:

1. Select a dark matter halo density profile parameterized by  $(\mu, \nu, \lambda)$

$$\rho_{\text{DM}}(r) = \frac{\delta_c \rho_{c0}}{x^\mu (1 + x^\nu)^\lambda}. \quad (52)$$

2. Fix  $B_p$  (eq. [44]),  $R$  (eq. [35]), and the polytropic exponent  $n$ .

3. Solve the following equation for  $\epsilon(x)$ :

$$\frac{d^2 \epsilon}{dx^2} + \frac{2}{x} \frac{d\epsilon}{dx} + B_p \left[ \frac{1}{x^\mu (1 + x^\nu)^\lambda} + R \epsilon^n \right] = 0, \quad (53)$$

with the boundary condition at  $x \ll 1$ ,

$$\epsilon(x) = 1 - \frac{B_p}{(2 - \mu)(3 - \mu)} x^{2-\mu}. \quad (54)$$

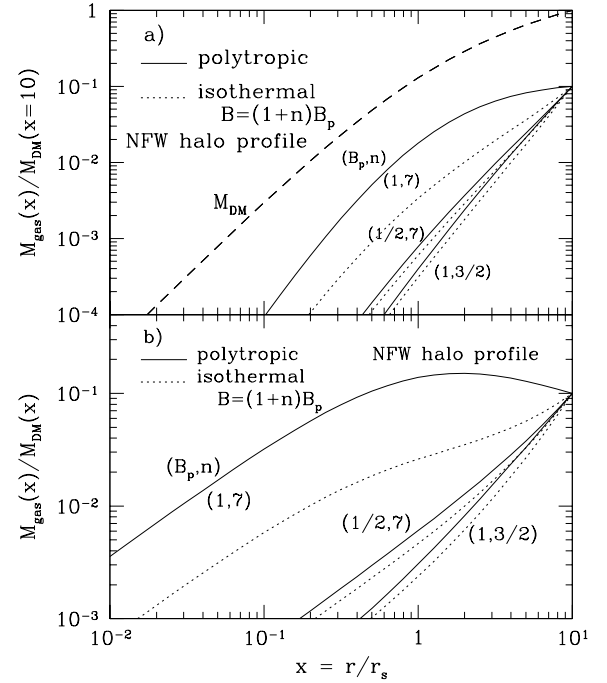


FIG. 6.—Mass profiles for polytropic models embedded in the NFW dark matter halo potential ( $\alpha = 1$ ) with  $(B_p, n) = (1.0, 7.0)$ ,  $(0.5, 7.0)$ , and  $(1.0, 1.5)$ . (a) Gas mass profiles for polytropic models (solid lines) and for the corresponding isothermal models (dotted lines) with  $B = (n+1)B_p$ . The gas mass is normalized to be 10% of the mass of dark matter halo at  $x = 10$ . The halo mass profile is plotted in dashed line for reference. (b) Gas-to-dark halo mass ratio for polytropic models (solid lines) and for the corresponding isothermal models (dotted lines) with  $B = (n+1)B_p$ .

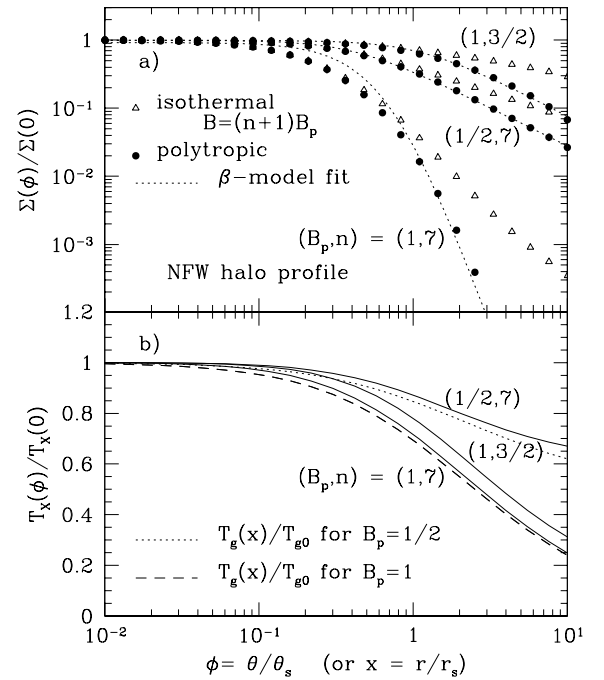


FIG. 7.—X-ray surface brightness and emission-weighted projected temperature profiles for polytropic models embedded in the NFW dark matter halo potential ( $\alpha = 1$ ) with  $(B_p, n) = (1.0, 7.0)$ ,  $(0.5, 7.0)$ , and  $(1.0, 1.5)$ . (a) Bolometric X-ray surface brightness (thermal bremsstrahlung only) profiles for polytropic models (filled circles) and for the corresponding isothermal models (open triangles) with  $B = (n+1)B_p$ . The dotted lines represent the best fits to the  $\beta$ -model. (b) Emission-weighted projected temperature profiles for polytropic models (solid lines), gas temperature with  $B_p = 1/2$  (dotted line), and  $B_p = 1$  (dashed line).

4. Then one obtains  $T_g(x) = T_{g0}\epsilon(x)$  and  $\rho_g(x) = \rho_{g0}[\epsilon(x)]^n$  and finally can compute the corresponding X-ray surface brightness  $\Sigma_x(\theta)$ , which should be compared with an appropriate sample of X-ray clusters.

5. Repeat the above procedure to determine the set of parameters  $\mu, v, \lambda, n, B_p$ , and  $R$ . The latter two quantities are combined to yield the amplitude of the halo density  $\delta_c \rho_{c0}$ .

With the current and future spatially resolved X-ray surface brightness and temperature profiles of several clusters of galaxies with *Einstein*, *ROSAT*, *ASCA*, *AXAF*, and *XMM*, the present methodology will be a useful tool in revealing the shape of the underlying dark matter halo

potential, which one has not been able to derive, and thus provide important information on theories of cosmic structure formation.

We thank the editor, E. L. Wright, for detailed and invaluable comments on our earlier manuscript. This research was supported in part by the Grants-in-Aid for the Center-of-Excellence (COE) Research of the Ministry of Education, Science, Sports, and Culture of Japan (07CE2002) to RESCEU (Research Center for the Early Universe), University of Tokyo, Japan.

#### REFERENCES

- Bardelli, S., Zucca, E., Malizia, A., Zamorani, G., Scaramella, R., & Vettolani, G. 1996, *A&A*, 305, 435  
 Bryan, G. L., & Norman, M. L. 1998, *ApJ*, 495, 80  
 Eke, V. R., Navarro, J. F., & Frenk, C. S. 1998, *ApJ*, 503, 569  
 Evans, N. W., & Collett, J. L. 1997, *ApJ*, 480, L103  
 Fukushige, T., & Makino, J. 1997, *ApJ*, 477, L9  
 Makino, N., & Asano, K. 1999, in press  
 Makino, N., Sasaki, S., & Suto, Y. 1998, *ApJ*, 497, 555 (Paper I)  
 Markevitch, M., Forman, W. R., Sarazin, C. L., & Vikhlinin, A. 1998, *ApJ*, 503, 77  
 Melott, A. L., Splinter, R. J., Shandarin, S. F., & Suto, Y. 1997, *ApJ*, 479, L79  
 Moore, B., Governato, F., Quinn, T., Stadel, J., & Lake, G. 1998, *ApJ*, 499, L5  
 Navarro, J. F., Frenk, C. S., & White, S. D. M. 1996, *ApJ*, 462, 563  
 ———. 1997, *ApJ*, 490, 493 (NFW)  
 Splinter, R. J., Melott, A. L., Shandarin, S. F., & Suto, Y. 1998, *ApJ*, 497, 38  
 Tamura, T. 1998, Ph.D. thesis, Univ. Tokyo  
 White, S. D. M., Navarro, J. F., Evrard, A. E., & Frenk, C. S. 1993, *Nature*, 366, 429  
 Xu, H., Makishima, K., Fukazawa, Y., Ikebe, Y., Kikuchi, K., Ohasi, T., & Tamura, T. 1998, *ApJ*, 500, 738  
 Yoshikawa, K., Itoh, M., & Suto, Y. 1998, *PASJ*, 50, 203